

Effects of Process Parameters on Microstructure and Properties of In-situ synthesized WC-reinforced Ni-based Cladding Layer

Cong-xiao Zhang^a , Wan-chang Sun^{a*} , Er-yong Liu^a, Yu-wan Liu^a , Jing-pei Liu^a ,
Bo Zhang^a, Meng-ran Zhou^a, Yi-fan Xu^a

^aXi'an University of Science and Technology, College of Materials Science and Engineering, 710054, Xi'an, Shaanxi, China.

Received: December 26, 2023; Revised: March 31, 2024; Accepted: April 14, 2024

A novel tungsten carbide (WC)-reinforced nickel (Ni)-based laser cladding layer was prepared through an in-situ synthesis process. The mechanism of the effect of scanning rates and laser power on the microstructures, wear and corrosion resistance of in-situ synthesized WC-reinforced Ni-based cladding layer were analyzed. The results revealed that the optimal in-situ synthesized WC laser cladding process entailed a scan rate of 3 mm/s and a laser power of 3000 W. The generation of WC phase has a significant strengthening effect on the cladding layer, which exhibits outstanding hardness (1261HV0.2). There is no clear linear relationship between scanning rate and abrasion resistance, and the coating abrasion resistance increased with increasing laser power. Furthermore, increasing the laser power improves the corrosion resistance of the cladding layer, while the scanning speed has a minimal effect on corrosion resistance.

Keywords: *Laser cladding, In-situ synthesized, Microstructure, Mechanical properties, Electrochemical properties.*

1. Introduction

Laser cladding stands out as a highly efficient method for acquiring composite coatings, enabling the development of cladding layers characterized by robust metallurgical bonding with the substrate and exceptional properties¹⁻³. Wear and corrosion resistance are the main challenges in the application of mining hydraulic support ball valves and coal mine interceptors, which operate in abrasive and corrosive environments⁴⁻⁶. Therefore, compared to improving the overall performance of the alloy material, constructing a coating on the surface of the material is an effective and economical method^{7,8}. The incorporation of ceramic particles into the laser cladding layer serves as an effective means of enhancing its properties⁹⁻¹¹. Moreover, the in-situ synthesis of reinforced phases presents a solution to various challenges encountered when directly doping hard phase particles, such as issues related to porosity and cracks^{12,13}. This approach not only improves the overall properties of the melted layer, including wear resistance and corrosion resistance^{14,15}, but also ensures a uniform distribution of reinforcement throughout the coating, resulting in excellent interfacial compatibility.

The doping of ceramic particles with hard phases can effectively enhance the performance of laser cladding layers. WC, as a primary reinforcing phase particle in metal matrix composites, offers remarkable properties including high chemical inertness, a low temperature expansion coefficient, exceptional hardness, excellent wear resistance, and good corrosion resistance^{16,17}. In addition to maintaining its

hardness at room temperature at high temperatures, is quite stable in high temperature processing and does not undergo phase transformation¹⁸. Nickel-based alloys are formed by incorporating various alloying elements into nickel, which hold significant practical value due to the excellent mechanical, physical, and chemical properties of nickel^{19,20}. Moreover, the ability to introduce components with diverse properties enables the creation of alloys tailored to specific requirements^{19,20}. In the melting process, Ni functions as a conventional binder and is dispersed at the interface of the WC hard-phase particles and acts as a strain energy dissipator during the service of the coating, while also improving the plasticity of the metal matrix composite.

Several studies have explored the impact of process parameters on laser cladding performance. However, it is crucial to select the appropriate laser cladding process based on the specific requirements of each application²¹⁻²³. Hu et al.²⁴ identified laser power, spot diameter, and scan rate as the primary factors influencing the height, width, and melt pool depth of the clad layer. Among these factors, laser power exhibited the most significant influence on microhardness, followed by spot diameter and scan rate. Excessive laser power can result in a rough structure of the molten layer, increased dilution rate, enhanced substrate melting, greater Fe content in the molten layer, and a decrease in its hardness. Marzban et al.²⁵ utilized statistical techniques to optimize laser cladding processes considering multiple performance characteristics such as cladding height, cladding width, and cladding depth. Their findings indicated that increasing laser power had a positive effect on cladding width but a negative

*e-mail: sunwanchang@tsinghua.org.cn

effect on cladding height and depth. Furthermore, increasing the scanning speed rate had a positive impact on all three parameters: cladding height, width, and depth.

In this study, WC-reinforced Ni-based laser cladding layers were constructed by in-situ synthesis process. The effects of different scanning rates and laser power on the microstructure, mechanical and electrochemical properties of laser cladding layer are compared and discussed.

2. Materials and Methods

2.1. Materials

2.1.1. Substrate material

The plate is selected as the base material for this test due to its improved cutting properties and higher comprehensive mechanical properties, including strength and toughness. To begin, the plate is wire cut into dimensions of 150 mm×90 mm×20 mm. Subsequently, the surface of the substrate is meticulously sanded using 400#, 800#, and 1000# sandpaper to achieve a smooth finish. Furthermore, the surface of the substrate is cleaned with anhydrous ethanol and blown dry for use. The chemical composition of AISI1045 plate is shown in Table 1.

2.1.2. Melting powder

The powders used for the cladding layer are Ni60 powder, WO₃ powder, B₄C powder and pure Al powder. The relevant parameters of the powder and the chemical composition and content of Ni60 powder are shown in Table 2.

2.2. Cladding layer preparation

The pre-configured molten powder was placed in a beaker according to a percentage of mass, a certain amount of anhydrous ethanol was added, and the powder was mechanically stirred for 4.5 h. Following this, the powder was transferred to a vacuum drying oven and subjected to drying at 90°C for 8 hours. Once dried, the powder was sealed and stored for future use.

In this experiment, the Ni-based laser cladding layer reinforced with in-situ synthesized WC ceramic particles was prepared using the pre-positioning method. By utilizing anhydrous ethanol as a binder, the dried powder was transformed into a paste and uniformly applied as a pre-coating on the surface of the AISI1045 plate. The pre-coating exhibited a thickness ranging from 1.5 to 2 mm and a width of 1.5 mm. Subsequently, the AISI1045 plate, along with the pre-placed metal powder, underwent preheating in a vacuum drying oven at 200°C for 4 hours. Once preheated, the plate was removed from the oven and the laser cladding equipment was utilized to prepare the cladding layer.

The BS-OF-3000-15-4L laser cladding machine of Xi'an Besam Laser Technology Co., Ltd. was selected to prepare in-situ synthesized WC-reinforced Ni-based cladding layers. The cladding equipment mainly consists of a laser system (laser head, cooler and control cabinet), a specialized cladding machine (three-dimensional translating and rotating mechanism), a gravity-fed powder system and an integrated control system. During normal operation, deionized water refrigeration and high-purity nitrogen dehumidification and real-time monitoring of its working status are provided. The standard output power of the laser is 3000 W, the spot size is 15mm × 2mm, and the main process parameters are shown in Table 3.

2.3. Characterization of the cladding layer

The surface and cross-sectional morphologies of cladding layer were viewed by using a scanning electron microscopy (SEM) microscope (JSM-6390A, Japan). The crystal phase of the cladding layer was analyzed by X-ray diffraction (XRD; XRD- 7000, Japan). The micro-indentation hardness of the cladding layer surface was measured by using a micro-Vickers hardness tester (EM-1500L, Shanghai Everone Ltd, China) under a load of 200 gram-force for 10 s. The final micro-indentation hardness is the statistical average of ten measurements conducted at different points with a space of 40 μm. The anti-wear features of the cladding layer were evaluated by using a friction and wear tester (MFT- R4000,

Table 1. The chemical composition and content of AISI1045 plate (wt.%).

C	Cr	Mn	Ni	P	S	Si	Fe
0.42-0.50	≤0.25	0.50-0.80	≤0.25	≤0.035	≤0.035	0.17-0.37	bal

Table 2. Powder related parameters.

(a) Cladding powder			
Power	Particle size	Purity	Manufacturer
Ni60	50-100μm	99.9%	Kennametal Stellite Co.,Ltd
WO ₃	25μm	99.9%	CMT Xindun Alloy Welding Spraying Co.,Ltd
B ₄ C	3.75μm /5μm /10μm/20μm	99.9%	Mudanjiang Jingangzuan Boron Carbide Co.,Ltd
Al	75μm	99.9%	Shanghai Hasu Industry & Trade Co.,Ltd
(b) The chemical composition and content of Ni60 powder (wt.%)			
C	Cr	Si	W
0.8	15.5	4	3

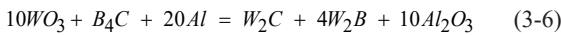
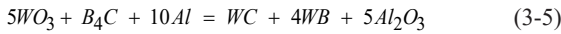
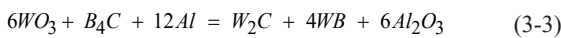
Lanzhou Huahui Instrument Technology Co., Ltd, China) at ambient temperature, and a GCr15 stainless steel ball with a diameter of 3.5 mm was run on the sample with a load of 25 N for 60 min. The corrosion resistance of the cladding layer was tested with an electrochemical workstation (PGSTAT302N, Aptar, Switzerland). The reference electrode used for the electrochemical experiments was a silver/silver chloride electrode, the counter electrode was a 20mm × 20mm platinum sheet, and the electrolyte was a 3.5 wt% sodium chloride solution.

3. Results and Discussion

3.1. Effect of process parameters on the microstructure of the cladding layer

3.1.1. Phase composition

The spontaneous reactions in the in-situ synthesized WC-reinforced Ni-based laser cladding layers are mainly as follows:



When laser cladding proceeds to the solidification process, a molten pool of W-C-Ni metal is generated²⁶. This molten pool establishes an optimal chemical-physical-metallurgical environment, facilitating the formation of necessary phases under favorable thermodynamic and dynamic conditions. With a melting point of 1453 °C for Ni²⁷, and both W and C boasting melting points exceeding 3000 °C, the Ni60 powder takes the lead in melting, forming the initial molten

pool. This, in turn, facilitates the complete fusion of C and W powders.

In the elevated temperature environment, C and W powders mutually dissolve, giving rise to WC cores. The process involves the absorption of surrounding C and W powders, resulting in the formation of larger WC particles. Based on thermodynamic data, the standard Gibbs formation free energy of WC (ΔG_f^0) is negative at 2000 K, indicating the spontaneous progression of the in-situ synthesis reaction of WC²⁶.

Figure 1 displays the XRD patterns of the In-situ synthesized WC-reinforced nickel-based cladding layers grown at different scan rates, with the laser power at 3000 W. The principal constituents of these cladding layers encompass the γ -(NiFe) solid solution, Al_2O_3 , W_2C , WC, WC_3 , WB_2 , WB_4 phases. Additionally, a minor presence of WC_{1-x} and $Cr_{23}C_6$ phases can be identified. Where the peak signal of WC occurs at (0001), (1010), (1011), (1121) and (1012).

The XRD results reveal that WC and W_2C hard phases are formed in situ at varying scan rates. When the scanning rate is 1 mm/s, the diffraction peak of WC phase appears weaker, while the diffraction peak of W_2C phase is stronger compared to other cladding layers. This disparity may be attributed to the decarburization and dissolution of WC particles under high heat input. However, with a gradual increase in the scan rate, the diffraction peak of the WC phase gradually strengthens, indicating an increased in-situ formation of WC. Simultaneously, the diffraction peaks of WB_4 and WB_2 also exhibit a gradual increase with the increase in scanning rate.

Figure 2 illustrates the XRD patterns of in-situ grown WC-reinforced Ni-based cladding layers with different laser powers with the scanning rate of 3 mm/s. The XRD patterns reveal that the primary phases present in the cladding layers at varying laser intensities consist of γ -(NiFe) solid solution, Al_2O_3 , WC, WC_3 , WB_2 and WB_4 phases, along with weaker phases of W_2C , WC_{1-x} and $Cr_{23}C_6$. Where the peak signal of WC occurs at (0001), (1010), (1011), (1121) and (1012). Notably, when the scanning power was set to 3000 W, the XRD pattern of the cladding layer exhibited a prominently visible WC diffraction peak. This observation suggests that at this specific laser power, the synthesis of WC particles reached its peak. It can be inferred that under different

Table 3. The main technical parameters of laser.

Sample number	Laser power(W)	Scanning rate(mm/s)
1	3000	1
2		2
3		3
4		4
5		5
6		6
7		7
8	1500	3
9	2000	
10	2500	
11	3000	

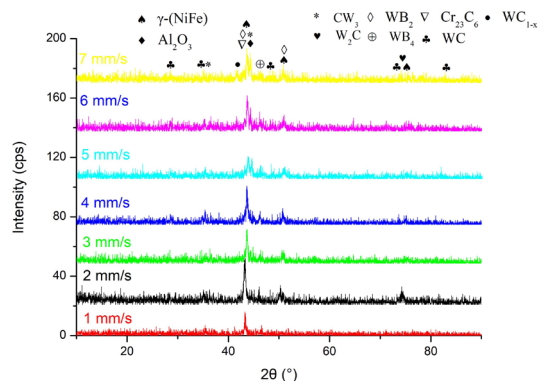


Figure 1. XRD patterns of in-situ grown WC reinforced nickel base cladding layer with different scanning rates.

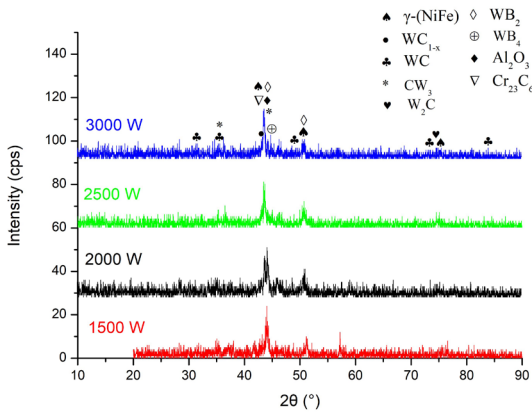


Figure 2. XRD patterns of in-situ grown WC reinforced nickel base cladding layer with different laser power.

laser powers, the in-situ growth of WC hard phases can be achieved, while the W_2C phase displays weaker diffraction peaks and lower levels of in-situ synthesis.

3.1.2. Microstructure

Figure 3 illustrates the cross-sectional morphology of the In-situ synthesized WC-reinforced nickel-based cladding layer, along with the microstructure of the upper, middle, and lower regions of the cladding layer at different scanning rates. The magnifications used for the images are 100 times, 1000 times, and 5000 times, respectively. Laser cladding is a process characterized by high heat input and rapid cooling, which significantly impacts the structural characteristics of the cladding layer. As depicted in Figure 3, a strong metallurgical bond is formed between the cladding layer and the substrate. Near the substrate, a segregation-free structure known as the “white bright band” area is observed. This phenomenon can be attributed to the dominant heat dissipation method being heat conduction near the substrate. Consequently, a large temperature gradient exists, but the solidification rate is relatively low, resulting in the growth of tissue at a slow and flat interface [99]. In the upper area of the cladding layer (indicated by the box in Figure 3), numerous small and dispersed black particles are present. These particles are likely generated by the in-situ reaction, leading to the formation of low-density W_2B and Al_2O_3 particles that float on the top of the cladding layer during the solidification process^{28,29}.

Figure 3(a) illustrates the columnar dendrites and a few equiaxed morphologies of the cladding layer when the scan rate was 1 mm/s. The high heat input during laser cladding resulted in a small amount of in-situ grown WC bulk particles in the cladding layer, with more in-situ grown WC found in the middle and bottom sections. Increasing the scanning rate to 2 mm/s led to a significant increase in in-situ grown WC bulk particles and improved coating hardness. However, the excessive heat input caused the dissolution of in-situ grown WC particles.

At a scanning rate of 3 mm/s, more In-situ synthesized WC hard phase particles were observed in the cladding layer, uniformly distributed throughout. The planar grain area at the bottom of the cladding layer was narrow. Prior to cladding, the cladding powder, including doped Al powder and B_4C

powder, was thoroughly mixed and stirred, ensuring even distribution in the cladding layer during the solidification process. This resulted in uniformly distributed nucleation particles of WC in the cladding layer, which continued to grow and solidify, forming an in-situ grown WC-reinforced nickel-based cladding layer with uniformly distributed WC particles.

Increasing the scan rate to 4 mm/s led to the appearance of secondary precipitates around the in-situ grown WC hard particles. The reduction in heat input caused decarburization of part of the WC phase, resulting in the formation of the W_2C phase and bright white lamellar W-rich layers at the edges of the WC hard phase particles. When the scanning rate exceeded 5 mm/s, a large number of butterfly-shaped precipitates formed due to the refinement and enrichment of WC particles in the cladding layer. Additionally, a wider plane crystal of the Fe and Ni diffusion layer appeared at the interface between the cladding layer and the substrate. Figure 3 (e4) and (f4) depict fine needle-like and rod-like precipitates in the dendrite area at the bottom of the cladding layer. This may be attributed to partial melting and reprecipitation of some in-situ grown WC particles, resulting in a lamellar W-rich eutectic structure. The butterfly-like structure significantly improved the hardness of the cladding layer. However, the low heat input caused inadequate bonding between the metal powder and the matrix, resulting in poor formability and an uneven surface of the cladding layer.

Figure 4 depicts the microstructure of the upper, middle, and lower regions of the in-situ grown WC-reinforced Ni-based cladding layer with different laser powers. The cladding layer exhibited a metallurgical bond with the substrate, and a dense planar crystal formed near the interface. As the liquid-solid interface progressed, the liquid temperature gradient decreased, resulting in increased component supercooling and growth rate of the crystal nucleus. This led to the gradual formation of a cellular crystal and dendrite structure. When the laser power was set at 1500 and 2000 W, the cladding layer primarily exhibited a butterfly-like structure. At 1500 W, a small amount of flower-like structure without a core was observed in the cladding layer, along with needle-like and rod-like structural precipitates in the middle and lower regions. When the laser power was increased to 2500 and 3000 W, the distribution of massive WC hard particles in the cladding layer became more uniform, with a significant increase in the number of WC particles as the laser power increased.

The appearance of the butterfly-like structure at lower laser power can be attributed to the refinement of in-situ grown WC particles and the enrichment of hard phases due to lower heat input. Additionally, the increase in laser power resulted in a significant improvement in the surface flatness and reduced unevenness of the cladding layer.

Figure 5 presents the EDS pattern of the In-situ synthesized WC-reinforced Ni-based cladding layer grown at a scan rate of 3 mm/s and a laser power of 3000 W. In Figure 5(a), it is evident that the atomic percentage of W and C elements in the white blocky particles within the cladding layer structure (box 1) is approximately 1:1, confirming that these white particles are WC hard particles. Conversely, the atomic percentage of Ni and Fe elements in the light gray phase of the cladding layer (box 2) is significantly higher than that

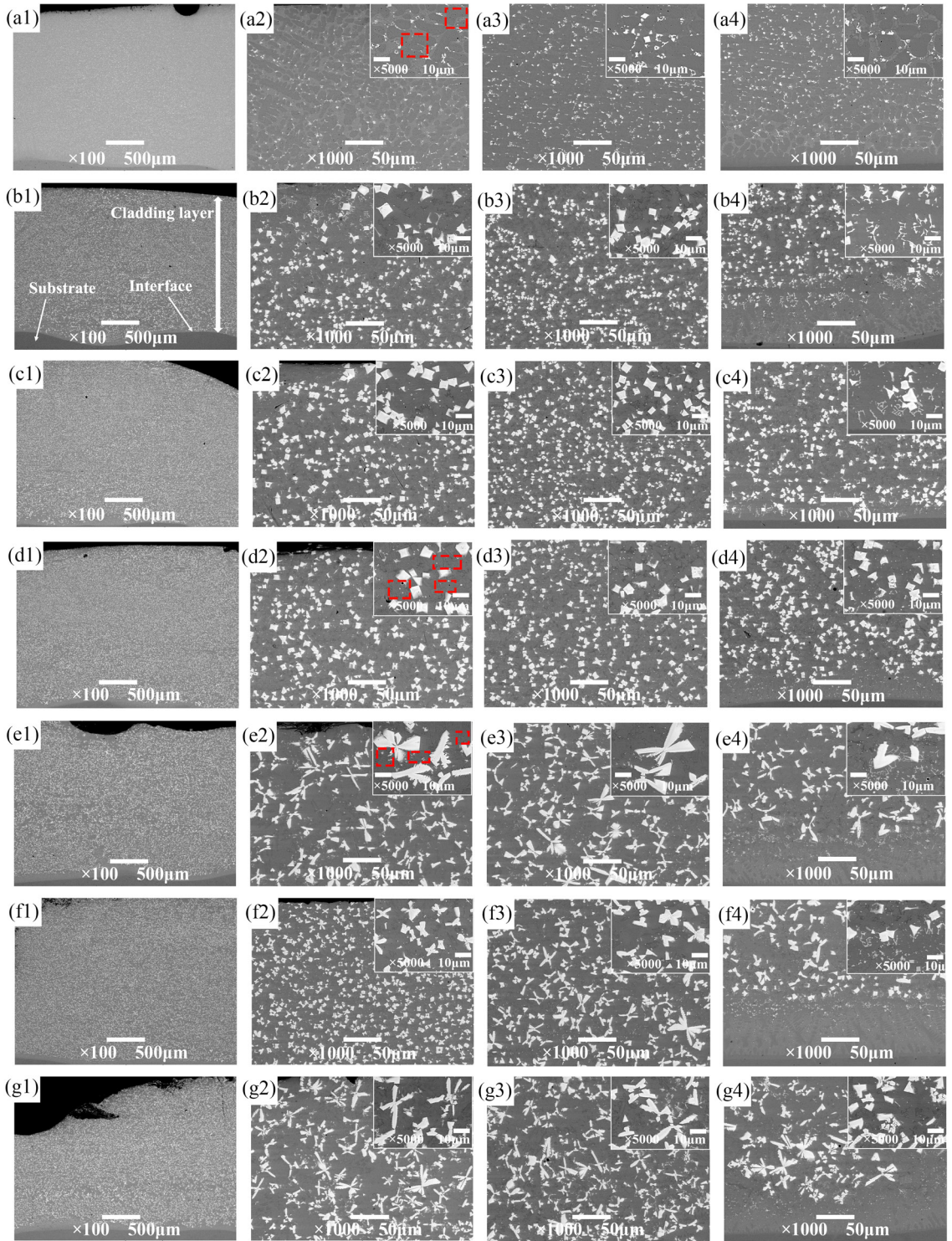


Figure 3. The microstructure morphologies of in-situ grown WC reinforced nickel base cladding layer with different scanning rates: (a) 1 mm/s, (b) 2 mm/s, (c) 3 mm/s, (d) 4 mm/s, (e) 5 mm/s, (f) 6 mm/s, (g) 7 mm/s; (1) cross-sectional panorama, (2) morphologies of the upper region, (3) morphologies of the middle region, (4) morphologies of the lower region.

of other elements, indicating that this phase is a γ -(NiFe) solid solution, serving as the matrix phase of the cladding layer. The dark gray phase in the cladding structure (arrow

3) exhibits a relatively balanced content of various elements, suggesting it may be an aggregated phase of Cr₂₃C₆ and other intermetallic compounds. Additionally, the white blocky

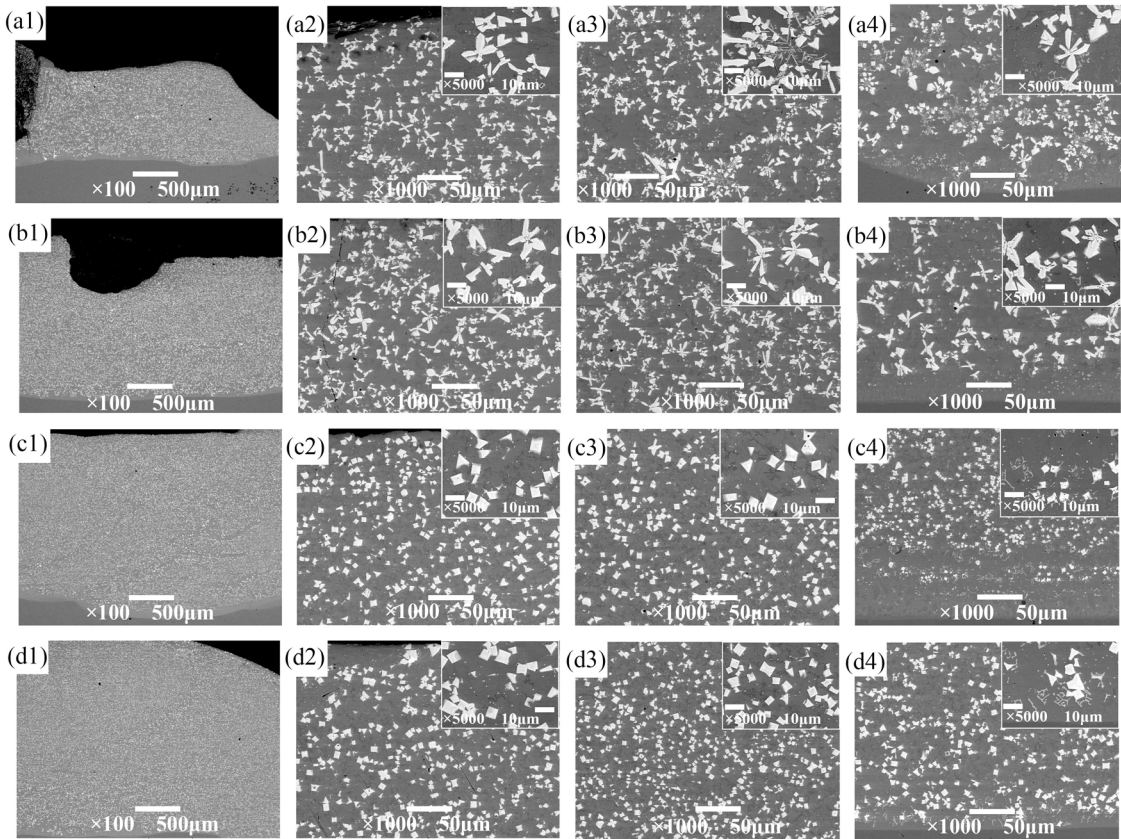


Figure 4. The microstructure morphologies of the upper/middle/lower region of in-situ grown WC reinforced nickel base cladding layer with different laser power: (a) 1500 W, (b) 2000 W, (c) 2500 W, (d) 3000 W; (1) cross-sectional panorama, (2) morphologies of the upper region, (3) morphologies of the middle region, (4) morphologies of the lower region.

particles display bright white edges, and the EDS spectrum analysis of these edges (arrow 4) reveals a significantly higher content of W element compared to other elements, indicating decarburization at the edges of WC hard particles and the formation of a W-rich phase.

In Figure 5(b), arrow 1 points to the AISI1045 matrix, primarily composed of Fe. In the bright zone area at the lower part of the cladding layer (arrows 2 and 4), it is observed that a portion of the matrix Fe element infiltrated into the coating, forming a composition transition zone. This further confirms the formation of an effective metallurgical bond between the substrate and the cladding layer. The gray-white phase in the lower region of the cladding layer (arrow 3) corresponds to a γ -(NiFe) solid solution. However, in the region close to the substrate, the Fe on the surface of the substrate melted and diffused into the cladding layer during the solidification process, resulting in a significantly higher Fe element content at the bottom of the cladding layer compared to other elements.

3.2. Effect of process parameters on hardness and friction and wear properties of cladding

3.2.1. Hardness

Figure 6 presents the histogram of the surface hardness of the In-situ synthesized WC-reinforced nickel-based

cladding layer grown at different scanning rates, while Figure 7 displays the cross-sectional hardness distribution curve of the cladding layer. In Figure 6, it is evident that the surface hardness of the cladding layer gradually increased with the scanning rate, reaching its peak at 5 mm/s with a hardness of 1261 HV0.2. Subsequently, as the scanning rate continued to increase, the hardness of the cladding layer slightly decreased to approximately 1180 HV0.2. This decrease can be attributed to the partial dissolution and decarburization of the in-situ grown WC and W₂C hard reinforcing phases at higher scanning rates. The gradually increasing butterfly-like structure in the cladding layer, which strengthens the material, contributes to the increased hardness when the scanning rate exceeds 5 mm/s.

Figure 7 demonstrates that the microhardness of the AISI1045 substrate, after undergoing normalizing treatment, was approximately 320 HV0.2. Comparatively, the in-situ grown WC-reinforced nickel-based laser cladding layer exhibited significantly improved hardness across different scanning rates, surpassing that of the AISI1045 substrate. Furthermore, the hardness distribution was relatively uniform from the interface between the substrate and the cladding layer to the surface of the cladding layer. This indicates that the in-situ growth of WC hard phase effectively addresses the issue of WC hard phase deposition solely on the bottom layer of the cladding layer when WC particles are directly doped.

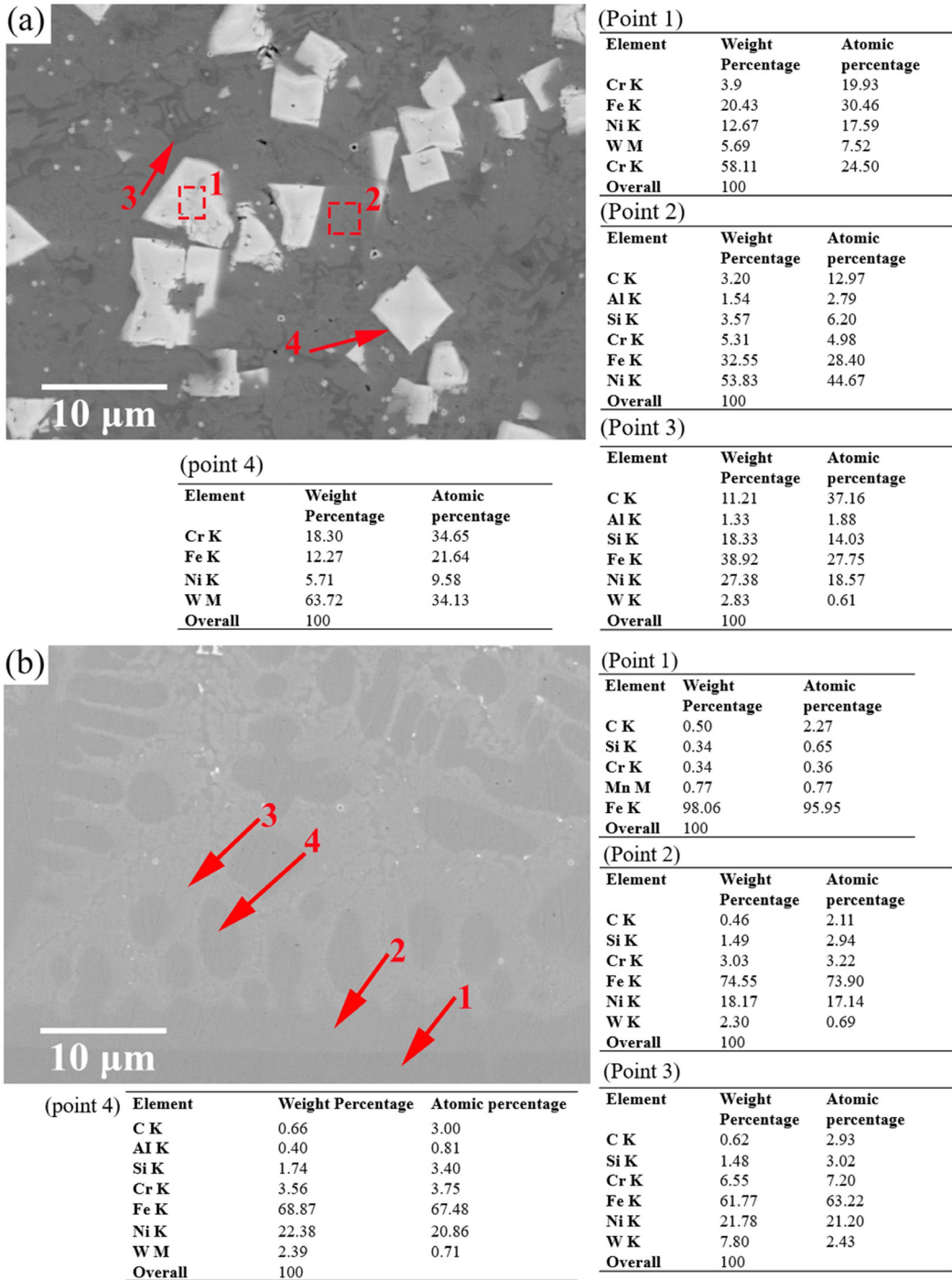


Figure 5. EDS spectrum of in-situ grown WC reinforced nickel base cladding layer with scanning rate of 3 mm/s and laser power of 3000 W: (a) the middle region, (b) the lower region.

Figure 8 depicts the histogram of the surface hardness of the in-situ grown WC laser cladding layer at different laser powers. Additionally, Figure 9 displays the cross-sectional hardness curve of the in-situ grown WC laser cladding layer under varying laser powers. It is evident from Figure 8 that the change in laser power has minimal impact on the hardness of the cladding layer. As the laser power increases, there

is a slight decrease in the hardness of the cladding layer. Figure 9 reveals that the hardness of the cladding layer, under each laser power, surpasses that of the substrate. Moreover, the hardness distribution from the interface to the surface of the cladding layer appears relatively uniform. Notably, the cladding layer with laser powers of 1500 and 2000 W exhibits greater hardness compared to the cladding layer

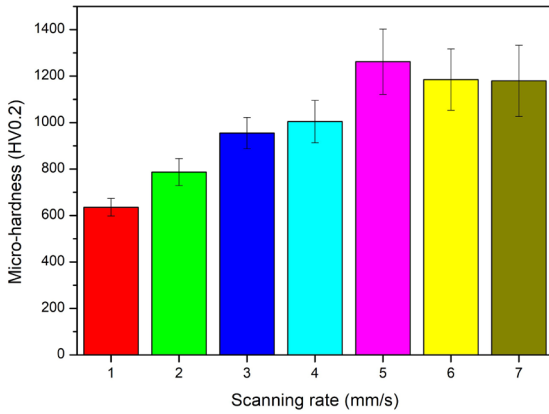


Figure 6. The surface hardness of in-situ grown WC reinforced nickel base cladding layer with different scanning rates.

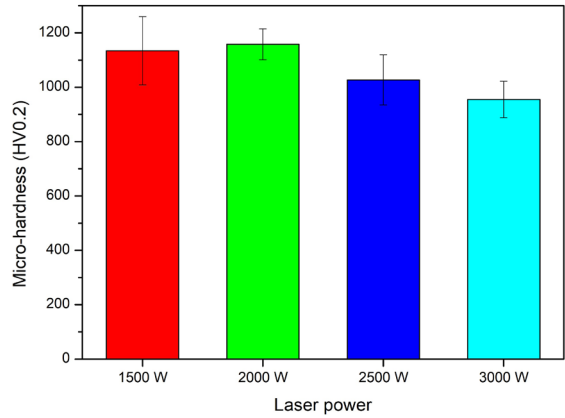


Figure 8. The surface hardness of in-situ grown WC reinforced nickel base cladding layer with different laser power.

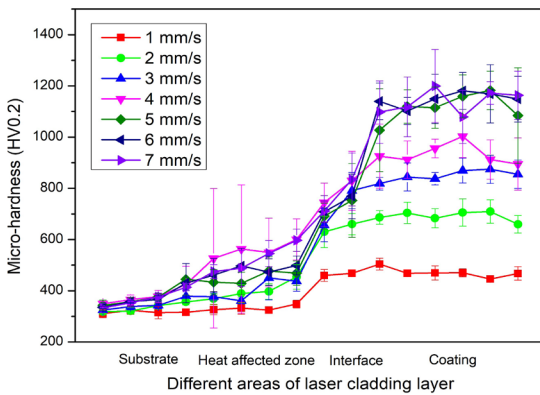


Figure 7. The cross-section hardness distribution of in-situ grown WC reinforced nickel base cladding layer with different scanning rates.

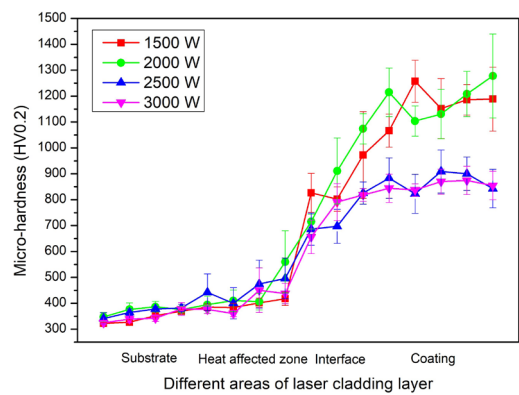


Figure 9. The cross-section hardness distribution of in-situ grown WC reinforced nickel base cladding layer with different laser power.

with laser powers of 2500 and 3000 W. This discrepancy may be attributed to the refinement and enrichment of the WC and W₂C hard reinforcing phases, resulting in the formation of butterfly-like structures at lower laser powers. These structures contribute to the enhancement of cladding layer hardness at lower laser powers.

3.2.2. Reciprocating friction and wear performance

Table 4 presents statistical data on the average friction coefficient and wear amount of the In-situ synthesized WC reinforced nickel-based cladding layer grown at different scanning rates. Additionally, Figures 10 and 11 illustrate the friction and wear curves, wear mechanism, and wear scar morphology of the cladding layer after friction and wear at varying scan rates, respectively. From Table 4 and Figure 10(a), it is evident that the wear resistance of the coating gradually increases with the scan rate until it reaches 4 mm/s. This improvement can be attributed to the gradual increase in WC hard phase particles within the cladding layer, significantly enhancing the wear resistance of the AISI1045 substrate surface. However, as the scan rate continues to increase, the wear resistance of the cladding

layer gradually decreases. At a scan rate of 6 mm/s, the wear resistance of the cladding layer is at its lowest. This decline may be attributed to the butterfly phase structure formed by the refinement and enrichment of the WC hard phase, which reduces the wear resistance of the substrate surface. However, when the scanning rate reaches 7 mm/s, the in-situ grown WC phase within the cladding layer undergoes significant refinement, effectively improving the wear resistance of the cladding layer.

Figure 11 reveals the presence of exfoliated holes, layered fragments, and noticeable grooves on the wear scar surface of the In-situ synthesized WC-reinforced Ni-based laser cladding layer. These observations indicate that the cladding layer undergoes plastic deformation during the wear process, leading to crack initiation and expansion, as well as micro-tears that exacerbate wear. At scanning rates exceeding 5 mm/s, the wear scar of the cladding layer exhibits a severe tear-like morphology. This can be attributed to the wear debris generated during friction and wear, which contains a significant number of detached massive WC hard particles and the precipitation phase of the butterfly-shaped structure. These factors contribute to cutting of the

Table 4. The friction coefficient and wear amount of in-situ grown WC reinforced nickel base cladding layer with different scanning rates.

Scan rate(mm/s)	1	2	3	4	5	6	7
Average coefficient of friction	0.190	0.165	0.179	0.292	0.387	0.561	0.272
Abrasion loss(mg)	1.9	1.7	0.7	2.0	1.5	1.2	0.6

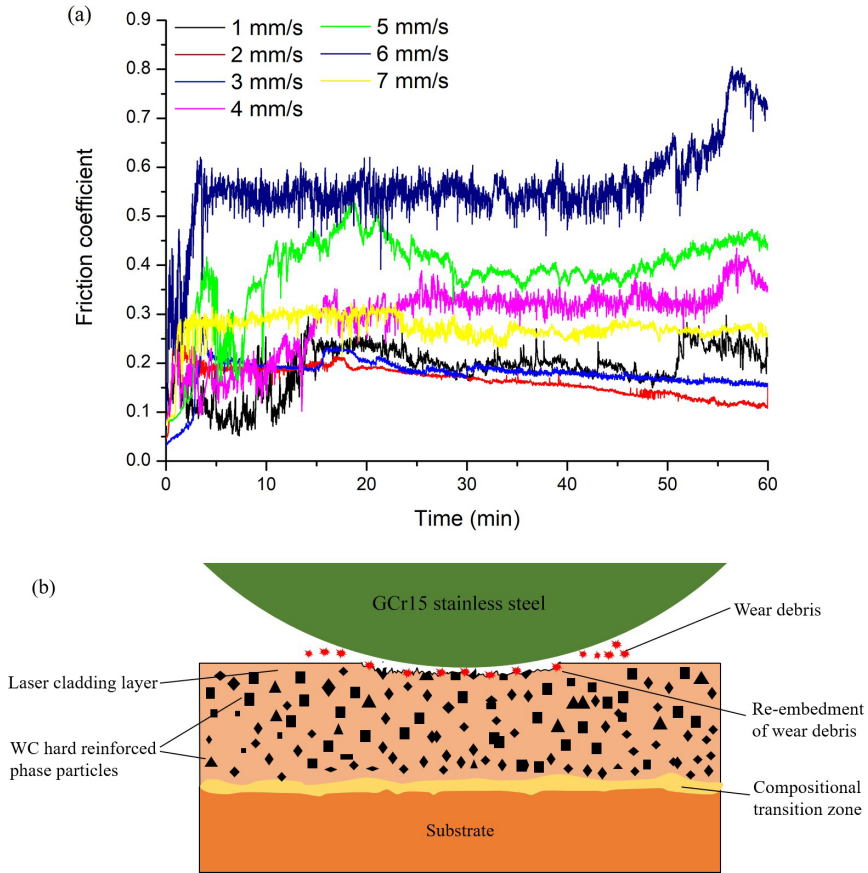


Figure 10. The friction coefficient curve and wear mechanism of in-situ grown WC reinforced nickel base cladding layer with different scanning rates: (a) friction coefficient, (b) wear mechanism.

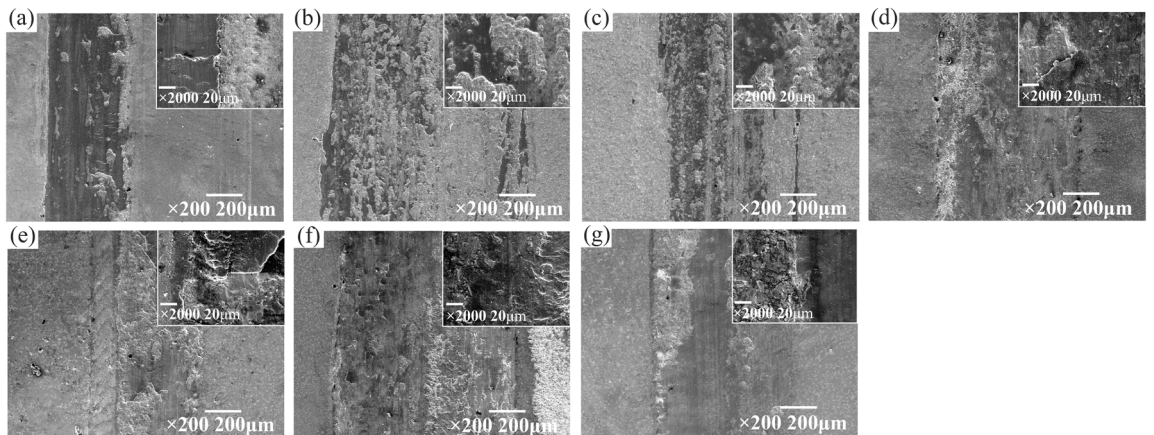


Figure 11. The wear scar morphologies of in-situ grown WC reinforced nickel base cladding layer with different scanning rates: (a) 1 mm/s, (b) 2 mm/s, (c) 3 mm/s, (d) 4 mm/s, (e) 5 mm/s, (f) 6 mm/s, (g) 7 mm/s.

cladding layer, secondary wear, and intensified friction and wear processes. Currently, the wear mechanism of the In-situ synthesized WC-reinforced nickel-based cladding layer primarily involves adhesive wear and abrasive wear, as depicted in Figure 10(b). During the friction and wear process, abrasive particles invade the cladding layer under the influence of a positive load, causing microscopic cutting of the WC particles and the matrix phase. Simultaneously, the tangential friction force affects the WC particles, while the matrix phase experiences adhesion-induced pulling forces. The matrix phase exhibits superior plasticity and toughness compared to the WC particles, resulting in plastic deformation of wear scars on the cladding layer surface until fracture occurs. Under the tangential friction, the edges of WC particles continuously absorb impact energy from the friction pair. When the force surpasses the critical brittle fracture load of WC, the WC particles crack and eventually detach. This process generates wear debris due to the instantaneous high temperature generated during friction.

Table 5 presents the statistics of the average friction coefficients for the in-situ grown WC cladding layers with different laser powers. Additionally, Figures 12 and 13 depict

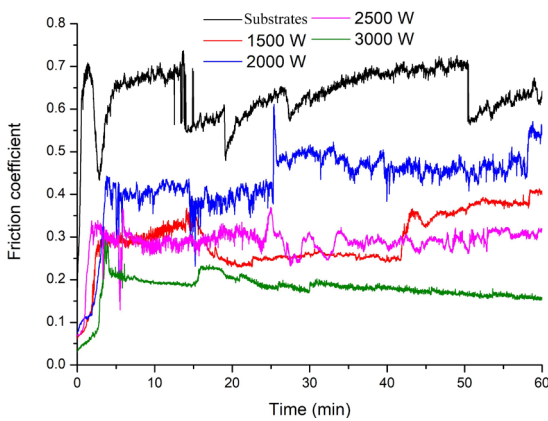


Figure 12. The friction coefficient curve of in-situ grown WC reinforced nickel base cladding layer with different laser power.

the friction coefficient curve and wear scar morphology of the in-situ grown WC-reinforced nickel-based cladding layer with varying laser powers after friction and wear, respectively. From Table 5 and Figure 12, it is evident that as the laser power increases, the wear resistance of the cladding layer gradually improves. This improvement can be attributed to the gradual increase in the amount of WC hard particles within the cladding layer, resulting in enhanced strengthening effects^{30,31}. At a laser power of 3000 W, the average friction coefficient of the cladding layer is only 0.179, with a wear amount of only 0.7 mg. This strengthening effect is more than twice that of the cladding layer at 2000 W. In comparison, the AISI1045 substrate exhibits an average friction coefficient of 0.635 and a wear amount of 3.3 mg, significantly higher than that of the other cladding layers. These findings demonstrate that the best wear resistance of the cladding layer was obtained at a laser power of 3000 W, which greatly improving the wear resistance of the substrate.

Figure 13 illustrates that during the friction and wear process, the in-situ grown WC hard particles tend to detach, leading to secondary wear on the cladding layer. The presence of lumpy hard particles causes cutting actions on the cladding layer, resulting in the formation of long and shallow furrows that exacerbate the wear process. Under the influence of counter-grinding materials, repeated extrusion and friction occur between the cladding layer and the counter-grinding ball, causing partial detachment of the hard phase, which adheres to the cladding layer's surface. At this stage, the wear mechanism of the cladding layer involves a combination of abrasive wear and adhesive wear.

The abrasion marks were widest when the laser power was 2000W, and obvious laminar spalling and deeper pits could be observed on the surface. When the laser power was 3000W, the width of the abrasion marks of the cladding layer was narrower, and the surface spalling was not as serious as that of the other three cladding layers. It is proved that the cladding layer had the best abrasion resistance when the laser power was 3000W.

As can be seen in Figure 4, when the laser power was 1500 W or 2000 W, the WC particles generated in the fusion cladding layer were irregularly shaped, mostly butterfly-

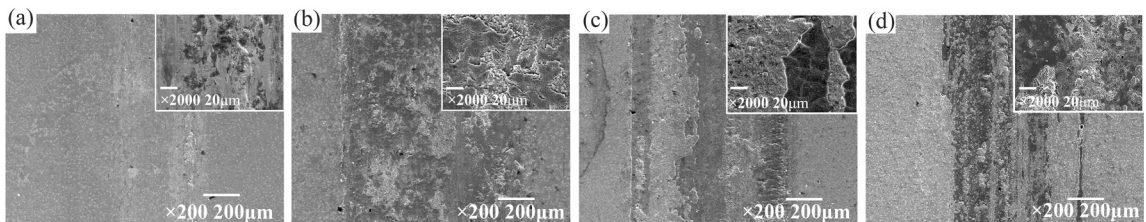


Figure 13. The wear scar morphologies of in-situ grown WC reinforced nickel base cladding layer with different laser power: (a) 1500 W, (b) 2000 W, (c) 12500 W, (d) 3000 W.

Table 5. The friction coefficient and wear amount of in-situ grown WC reinforced nickel base cladding layer with different laser power.

Laser power(W)	Substrate	1500	2000	2500	3000
Average coefficient of friction	0.635	0.294	0.428	0.288	0.179
Abrasion loss(g)	3.3	1.7	2.3	0.8	0.7

shaped, while the WC particles generated at 2500 W and 3000 W were mostly regular shapes of quadrilateral or triangular shape. This indicates that regular WC particles can enhance the wear resistance of the coating, the reason may be that WC particles were shed during the friction process, and the irregular butterfly-shaped particles caused more serious secondary wear.

Overall, the effects of different scanning rates on the friction and wear properties of the cladding layer were not obvious enough, showing the best wear resistance at 3 mm/s. The effects of laser power on the friction properties of the cladding layer showed a linear relationship, and the wear resistance increased with the increase of laser power, and the best wear resistance of the cladding layer was achieved at 3000W.

3.3. Effect of process parameters on electrochemical properties of cladding layer

Figure 14 presents the polarization curves, impedance diagrams, and bode diagrams of the In-situ synthesized WC-reinforced nickel-based cladding layers grown at different scan rates. The self-corrosion current density (I_{corr}) serves as an indicator of the material's corrosion degree, with higher values indicating deeper corrosion and poorer corrosion resistance of the cladding layer. In the fitted circuit, CPE1, CPE2, $R_{\text{ct}1}$, $R_{\text{ct}2}$ and R_s represent the coating capacitance, double-layer interface capacitance, coating resistance, charge transfer resistance, and solution resistance, respectively³². The corrosion resistance of the coatings is closely related to $R_{\text{ct}1}$ and $R_{\text{ct}2}$, where larger values of $R_{\text{ct}1}$ and $R_{\text{ct}2}$ generally

indicate lower corrosion rates^{33,34}. From Figure 14(a), it can be observed that there is no significant linear relationship between the self-corrosion current density of the cladding layer and the scanning rate, indicating that the scanning rate has little effect on the corrosion resistance of the cladding layer. Among all the cladding layers, the lowest self-corrosion current density was observed at 3.6853×10^{-8} and 1.6525×10^{-8} A/cm² when the scan rate was 4 and 6 mm/s, respectively. These results indicate better corrosion resistance of the cladding layer at these scan rates. However, when the scanning rate reached 7 mm/s, the cladding layer exhibited a maximum self-corrosion current density of 1.1887×10^{-5} A/cm², indicating poor corrosion resistance.

Figure 14(a) indicates that passivation occurred in the polarization curves of the cladding layers at scan rates of 1-6 mm/s. In this range, the current density temporarily stabilized or decreased as the potential increased. The in-situ grown WC-reinforced nickel-based cladding layer rapidly developed passivation films on its surface in corrosive environments, making the cladding layer enter the passivation zone and significantly reduce or no longer increase the self-corrosion current density. The passivation film formed during this process was in a dynamic equilibrium, continuously undergoing dissolution, destruction, and regeneration. The presence of Cr_2O_3 and Al_2O_3 oxide passivation films on the surface of the cladding layer limited the entry of corrosive liquids into the coating/substrate interface, effectively slowing down the corrosion of the coating surface.

In Figure 14(b), (c), it can be observed that at a scan rate of 4 mm/s, the cladding layer exhibited the largest arc

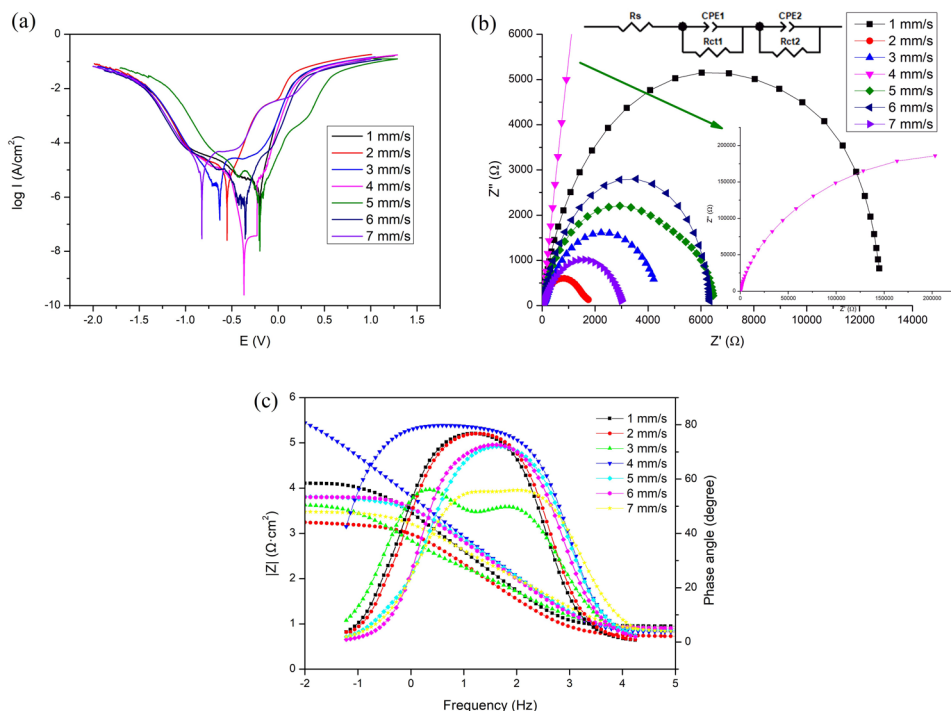


Figure 14. The electrochemical properties of in-situ grown WC reinforced nickel base cladding layer with different scanning rates: (a) polarization curve, (b) impedance diagram, (c) bode diagram.

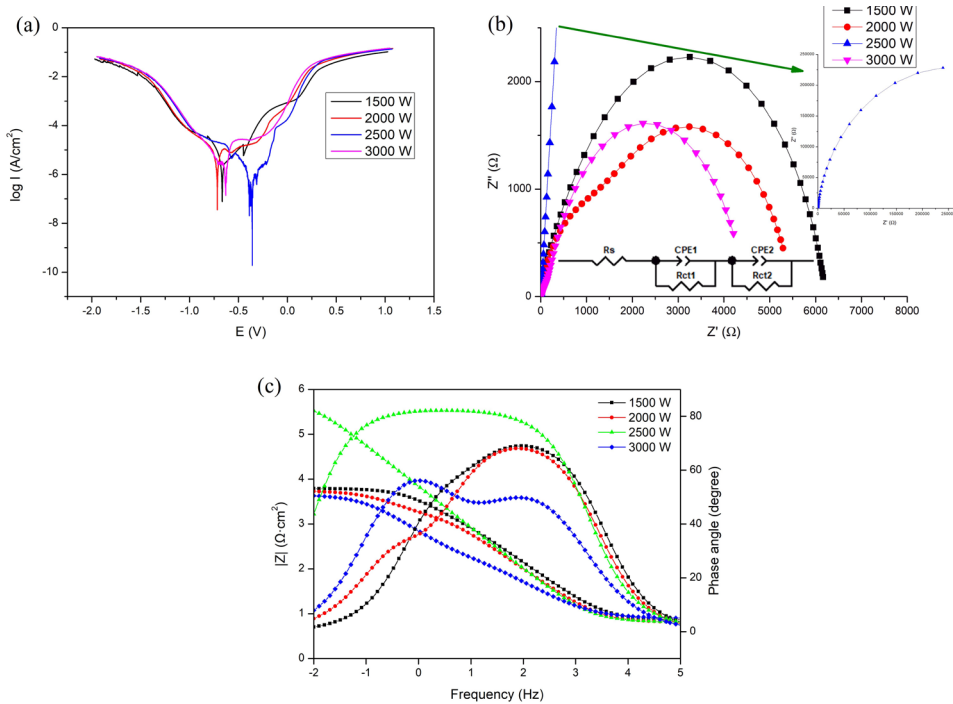


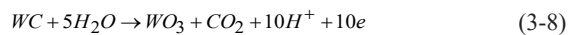
Figure 15. The electrochemical properties of in-situ grown WC reinforced nickel base cladding layer with different laser power: (a) polarization curve, (b) impedance diagram, (c) bode diagram.

radius of capacitive reactance. The solution resistance of the cladding layer was measured to be $6.502 \cdot 6.502 \Omega \cdot \text{cm}^2$, while the coating resistance and charge transfer resistance were 101990 and $311670 \cdot 6.502 \Omega \cdot \text{cm}^2$, respectively. The coating capacitance and double-layer interface capacitance were determined to be 5.1397×10^{-5} and $6.1049 \times 10^{-5} \Omega^{-1} \text{S} \cdot \text{cm}^2$, respectively. These findings indicate that the charge transfer resistance of the cladding layer at a scan rate of 4 mm/s was the highest, making it more resistant to material corrosion.

Figure 15 displays the impedance diagram and bode diagram of the in-situ growth of WC-reinforced nickel-based cladding layers at different laser powers. Analysis of Figure 15(a) reveals that the cladding layer exhibited noticeable passivation under varying laser powers, effectively delaying the corrosion process. The combination of Figure 15 indicates that the corrosion resistance of the cladding layer improved with increasing laser power. This suggests that higher laser power resulted in a gradual increase in the WC hard phase within the cladding layer, thereby enhancing its corrosion resistance.

The cladding layer with the highest corrosion resistance was prepared using a laser power of 2500 W . It exhibited a self-corrosion current density of $5.1549 \times 10^{-8} \text{ A/cm}^2$, and its capacitive reactance had a significantly larger arc radius compared to other cladding layers. Additionally, the coating resistance and charge transfer resistance were measured at 259680 and $520650 \Omega \cdot \text{cm}^2$, respectively. The cladding layer with a laser power of 3000 W demonstrated slightly weaker corrosion resistance than the 2500 W cladding layer, but still outperformed the cladding layers with laser powers of 1500 and 2000 W . This suggests that the butterfly-shaped

structure did not enhance the corrosion resistance of the cladding layer as effectively as the presence of massive WC particles. The reaction equation for electrochemical corrosion of WC phase in NaCl solution are as follows:



Electrochemical corrosion of the WC phase produces OH^- , which leads to a localized increase in the pH of the corrosion solution, leaving the internal WC particles in a locally alkaline environment, which in turn leads to the dissolution of part of the WC phase³⁵⁻³⁷. It is hypothesized that the electrochemical reaction is more intense because the butterfly-shaped WC particles have a larger contact area.

4. Conclusion

In this paper, In-situ synthesized WC-reinforced nickel-based cladding layers were prepared, and the effects of different scanning rates and laser powers on the microstructure, mechanical properties and corrosion resistance of the coatings were investigated. The main conclusions are summarized below:

- (1) The results indicate that the optimal in-situ growth WC laser cladding process involved a laser power of 3000 W and a scanning rate of 3 mm/s . Under these conditions, the cladding layer exhibited a dense structure without defects such as pores and

cracks. Furthermore, there was a good metallurgical combination with the base material.

- (2) At lower scanning rates, in-situ grown WC bulk particles were only present in low quantities within the cladding layer. As the scanning rate increased, a significant number of uniformly distributed white in-situ grown WC bulk particles appeared. When the scanning rate exceeded 5 mm/s, butterfly-shaped structural precipitates became prominent in the cladding layer. Additionally, when the laser power was lower, butterfly-like structural precipitates formed due to the refinement and enrichment of hard phases. As the laser power increased, a substantial amount of white in-situ grown WC bulk particles were dispersed throughout the cladding layer.
- (3) Regarding hardness, the cladding layer exhibited a maximum hardness of 1261 HV0.2. There is no obvious linear relationship between the scanning rate and the abrasion resistance of the coating, and the abrasion resistance was best when the scanning rate was 3-4 mm/s; the wear resistance of the cladding layer increased gradually with higher laser powers, and the cladding layer had the best abrasion resistance when the laser power was 3000W.
- (4) The scan rate had minimal impact on the corrosion resistance of the cladding layer, while an increase in laser power improved corrosion resistance. The best corrosion resistance was observed at a scan rate of 4 mm/s and a laser power of 2500 W.

5. Acknowledgments

The work was supported by the key research and development project of Shaanxi Province [Grant No. 2021SF-469] and the National Natural Science Foundation of China [Grant No.52175184].

6. References

1. Li B, Zhu H, Qiu C, Gong X. Laser cladding and in-situ nitriding of martensitic stainless steel coating with striking performance. *J Mater Lett.* 2020;259:126829. <http://doi.org/10.1016/j.matlet.2019.126829>.
2. Zhu H, Li Y, Li B, Zhang Z, Qiu C. Effects of Lo30w-temperature tempering on microstructure and properties of the laser-cladded AISI 420 martensitic stainless steel coating. *Coatings.* 2018;8(12):451. <http://doi.org/10.3390/coatings8120451>.
3. Huang L, Zhou J, Xu J, Huo K, He W, Meng X, Huang S. Microstructure and wear resistance of electromagnetic field assisted multi-layer laser clad Fe901 coating. *J Surf Coat Technol.* 2020;395:125876. <http://doi.org/10.1016/j.surfcoat.2020.125876>.
4. Li BC, Zhu HM, Qiu CJ, Zhang DK. Development of high strength and ductile martensitic stainless steel coatings with Nb addition fabricated by laser cladding - ScienceDirect. *J Alloys Compd.* 2020;832:154985. <http://doi.org/10.1016/j.jallcom.2020.154985>.
5. Lian G, Zhang H, Zhang Y, Chen C, Huang X, Jiang J. Control and prediction of forming quality in curved surface multi-track laser cladding with curve paths. *Int J Adv Manuf Technol.* 2020;106(9-10):3669-82. <http://doi.org/10.1007/s00170-019-04893-7>.
6. Zhang Z, Yu T, Kovacevic R. Erosion and corrosion resistance of laser cladded aisi 420 stainless steel reinforced with VC. *Appl Surf Sci.* 2017;410:225-40. <http://doi.org/10.1016/j.apsusc.2017.03.137>.
7. Wang K, Chang B, Chen J, Fu H, Lin Y, Lei Y. Effect of molybdenum on the microstructures and properties of stainless steel coatings by laser cladding. *Appl Sci (Basel).* 2017;7(10):1065. <http://doi.org/10.3390/app7101065>.
8. Nath SD, Clinning E, Gupta G, Wuelfrath-Poirier V, L'Espérance G, Gulsoy O, et al. Effects of Nb and Mo on the microstructure and properties of 420 stainless steel processed by laser-powder bed fusion. *Addit Manuf.* 2019;28:682-91. <http://doi.org/10.1016/j.addma.2019.06.016>.
9. Zhang DW, Zhang XP. Laser cladding of stainless steel with Ni-Cr₃C₂ and Ni-WC for improving erosive-corrosive wear performance. *Surf Coat Tech.* 2005;2/3(2-3):190. <http://doi.org/10.1016/j.surfcoat.2004.03.018>.
10. Xiang K, Chen L-Y, Chai L, Guo N, Wang H. Microstructural characteristics and properties of CoCrFeNiNb_x high-entropy alloy coatings on pure titanium substrate by pulsed laser cladding. *Appl Surf Sci.* 2020;517:146214. <http://doi.org/10.1016/j.apsusc.2020.146214>.
11. Li M., Han B., Song L., He O. Enhanced surface layers by laser cladding and ion sulfurization processing towards improved wear-resistance and self-lubrication performances. *J Appl Surf Sci.* 2020;503:144226. <http://doi.org/10.1016/j.apsusc.2019.144226>.
12. Rong T, Gu D, Shi Q, Cao S, Xia M. Effects of tailored gradient interface on wear properties of WC /Inconel 718 composites using selective laser melting. *Surf Coat Tech.* 2016;307:418-27. <http://doi.org/10.1016/j.surfcoat.2016.09.011>.
13. Karmakar GMDP, Nath AK. In-process detection of microstructural changes in laser cladding of in-situ Inconel 718/TiC metal matrix composite coating. *J Alloys Compd.* 2018;740:545-58. <http://doi.org/10.1016/j.jallcom.2017.12.364>.
14. Hong S, Wu Y, Li G, Wang B, Gao W, Ying G. Microstructural characteristics of high-velocity oxygen-fuel (HVOF) sprayed nickel-based alloy coating. *J Alloys Compd.* 2013;581:398-403. <http://doi.org/10.1016/j.jallcom.2013.07.109>.
15. Bolelli G, Berger L-M, Bonetti M, Lusvardi L. Comparative study of the dry sliding wear behaviour of HVOF-sprayed WC-(W,Cr)2C-Ni and WC-CoCr hardmetal coatings. *Wear.* 2014;309(1-2):96-111. <http://doi.org/10.1016/j.wear.2013.11.001>.
16. Xiao Q, Sun W, Yang K, Xing X, Chen Z, Zhou H, et al. Wear mechanisms and micro-evaluation on WC particles investigation of WC-Fe composite coatings fabricated by laser cladding. *Surf Coat Tech.* 2021;420(9):127341. <http://doi.org/10.1016/j.surfcoat.2021.127341>.
17. Liu YW, Sun WC, Tian SS, Jia Y, Xiao Y. Microstructures and high-temperature friction and wear behavior of high-velocity oxygen-fuel-sprayed WC-12%Co-6%Cr coatings before and after sealing. *J Mater Eng Perform.* 2020;31(1):448-60. <http://doi.org/10.1007/s11665-021-06167-4>.
18. Gu D, Shen Y. Microstructures and properties of direct laser sintered tungsten carbide (WC) particle reinforced Cu matrix composites with RE-Si-Fe addition: a comparative study. *J Mater Res.* 2009;24(11):3397-406. <http://doi.org/10.1557/jmr.2009.0419>.
19. Zhai LL, Ban CY, Zhang JW. Investigation on laser cladding Ni-base coating assisted by electromagnetic field. *Opt Laser Technol.* 2019;114:81-8. <http://doi.org/10.1016/j.optlastec.2019.01.017>.
20. Ding L, Hu S, Quan X, Shen J. Effect of Mo and nano-Nd2O3 on the microstructure and wear resistance of laser cladding Ni-based alloy coatings. *Appl Phys, A Mater Sci Process.* 2016;122(4pt 1):1-7. <http://doi.org/10.1007/s00339-016-9905-1>.
21. Sun Y, Hao M. Statistical analysis and optimization of process parameters in Ti6Al4V laser cladding using Nd:YAG laser. *Opt Lasers Eng.* 2012;50(7):985-95. <http://doi.org/10.1016/j.optlaseng.2012.01.018>.
22. Liu YH, Guo ZX, Yang Y, Wang HY, Hu JD, Li YX, et al. Laser (a pulsed Nd:YAG) cladding of AZ91D magnesium alloy with Al and Al2O3 powders. *Appl Surf Sci.* 2006;253(4):1722-8. <http://doi.org/10.1016/j.apsusc.2006.03.003>.

23. Lee HK. Effects of the cladding parameters on the deposition efficiency in pulsed Nd:YAG laser cladding. *J Mater Process Technol.* 2008;202(1-3):321-7. <http://doi.org/10.1016/j.jmatprotec.2007.09.024>.
24. Hu G, Yang Y, Qi K, Lu X, Li J. Investigation of the microstructure and properties of niCrBSi coating obtained by laser cladding with different process parameters. *Trans Indian Inst Met.* 2020;73(10):2623-34. <http://doi.org/10.1007/s12666-020-02065-w>.
25. Marzban J, Ghaseminejad P, Ahmadzadeh MH, Teimouri R. Experimental investigation and statistical optimization of laser surface cladding parameters. *Int J Adv Manuf Tech.* 2015;76:1163-72. <http://doi.org/10.1007/s00170-014-6338-x>.
26. Bogue R. Fifty years of the laser: its role in material processing. *Assem Autom.* 2010;30(4):317-22. <http://doi.org/10.1108/01445151011075771>.
27. Zhong M, Liu W, Zhang Y, Zhu X. Formation of WC/Ni hard alloy coating by laser cladding of WC/Ni pure element powder blend. *Int J Refract Hard Met.* 2006;24(6):453-60. <http://doi.org/10.1016/j.ijrmhm.2005.09.002>.
28. Luo D, Hellman J, Luhulima D, Liimatainen J, Lindroos VK. Interactions between tungsten carbide (WC) particulates and metal matrix in WC-reinforced composites. *Mater Sci Eng A.* 2003;340(1-2):155-62. [http://doi.org/10.1016/S0921-5093\(02\)00173-9](http://doi.org/10.1016/S0921-5093(02)00173-9).
29. Prywer J. Explanation of some peculiarities of crystal morphology deduced from the BFDH law. *J Cryst Growth.* 2004;270(3-4):699-710. <http://doi.org/10.1016/j.jcrysgro.2004.06.046>.
30. Tjong SC, Ma ZY. Microstructural and mechanical characteristics of in situ metal matrix composites [J]. *Mater Sci Eng Rep.* 2000;29(3):49-113. [http://doi.org/10.1016/S0927-796X\(00\)00024-3](http://doi.org/10.1016/S0927-796X(00)00024-3).
31. Yang C, Jing CN, Fu TL, Lin T, Guo W, Liu N. Effect of CeO₂ on the microstructure and properties of AlCoCrFeNi_{2.1} laser cladding coatings. *J Alloys Compd.* 2024;976:172948. <http://doi.org/10.1016/j.jallcom.2023.172948>.
32. Zheng H, Shao Y, Wang Y, Meng G, Liu B. Reinforcing the corrosion protection property of epoxy coating by using graphene oxide-poly(urea-formaldehyde) composites. *Corros Sci.* 2017;123:267-77. <http://doi.org/10.1016/j.corsci.2017.04.019>.
33. Do Q, An H, Wang G, Meng G, Wang Y, Liu B, et al. Effect of cupric sulfate on the microstructure and corrosion behavior of nickel-copper nanostructure coatings synthesized by pulsed electrodeposition technique. *Corros Sci.* 2018;147:246-59. <http://doi.org/10.1016/j.corsci.2018.11.017>.
34. Aliyu A, Rekha MY, Srivastava C. Microstructure-electrochemical property correlation in electrodeposited CuFeNiCoCr high-entropy alloy-graphene oxide composite coatings. *Philos Mag.* 2018;1-18. <http://doi.org/10.1080/14786435.2018.1554915>.
35. Ghosh G, Sidpara A, Bandyopadhyay PP. Understanding the role of surface roughness on the tribological performance and corrosion resistance of WC-Co coating. *Surf Coat Tech.* 2019;378:125080. <http://doi.org/10.1016/j.surfcoat.2019.125080>.
36. Zhai L, Ban C, Zhang JW. Microstructure, microhardness and corrosion resistance of NiCrBSi coatings under electromagnetic field auxiliary laser cladding. *Surf Coat Tech.* 2019;358:531-8. <http://doi.org/10.1016/j.surfcoat.2018.11.034>.
37. Hosseini N, Karimzadeh F, Abbasi MH, Choi GM. Correlation between microstructure and electrical properties of Cu_{1.3}Mn_{1.7}O₄/La₂O₃ composite-coated ferritic stainless steel interconnects. *J Alloys Compd.* 2016;673:249-57. <http://doi.org/10.1016/j.jallcom.2016.02.249>.